Hybrid PIC–fluid simulations for fast electron transport in a silicon target

View Online   Export Citation   CrossMark

X. H. Yang[1,2,a)] 🆔 Z. H. Chen[1] 🆔 H. Xu[2,3,b)] Y. Y. Ma[2,4] 🆔 G. B. Zhang[1] D. B. Zou[5] 🆔 and F. Q. Shao[5] 🆔

AFFILIATIONS

[1] Department of Nuclear Science and Technology, National University of Defense Technology, Changsha 410073, China
[2] Collaborative Innovation Center of IFSA, Shanghai Jiao Tong University, Shanghai 200240, China
[3] School of Computer Science, National University of Defense Technology, Changsha 410073, China
[4] College of Advanced Interdisciplinary Studies, National University of Defense Technology, Changsha 410073, China
[5] Department of Physics, National University of Defense Technology, Changsha 410073, China

[a)] Author to whom correspondence should be addressed: xhyang@nudt.edu.cn
[b)] Electronic mail: xuhan_email@aliyun.com

ABSTRACT

Ultra-intense laser-driven fast electron beam propagation in a silicon target is studied by three-dimensional hybrid particle-in-cell–fluid simulations. It is found that the transverse spatial profile of the fast electron beam has a significant influence on the propagation of the fast electrons. In the case of a steep spatial profile (e.g., a super-Gaussian profile), a tight fast electron beam is produced, and this excites more intense resistive magnetic fields, which pinch the electron beam strongly, leading to strong filamentation of the beam. By contrast, as the gradient of the spatial profile becomes more gentle (e.g., in the case of a Lorentzian profile), the resistive magnetic field and filamentation become weaker. This indicates that fast electron propagation in a solid target can be controlled by modulating the spatial gradient of the laser pulse edge.

I. INTRODUCTION

Collimated propagation of an ultra-intense laser-driven fast electron beam in a target is critical to many applications, such as fast ignition schemes in inertial confinement fusion.[1] However, it is not easy to realize high-quality fast electron beam transport in dense plasmas owing to the accompanying large initial divergence[2–4] and beam–plasma instabilities.[5–8]

Various methods have been proposed to control fast electron propagation in targets.[9–13] One of the most commonly used is optimized design of target structures, such as double-cone,[14,15] cone–channel,[16] cone–wire,[17] and sandwich[18] targets. In these cases, a strong quasi-static magnetic field or electrostatic field can be excited during the fast electron transport through the target and confine the fast electron beam. The fields are produced by fast electrons escaping from or refluxing around the target surface in the first three cases, and the fast electron beam is controlled by the balance between the magnetic field and the electric field. With a sandwich

target, the fast electrons are collimated by the resistive magnetic field generated by the resistivity gradient around the target material interface. To enhance the resistive magnetic field, we have proposed a scheme in which a low-Z target is doped with high-Z materials.[19] The gradients of both target resistivity and density are modulated in this way, and the fast electron propagation is improved. We found that in addition to the strength of the resistive magnetic field, the magnetic field structure is also important for collimated propagation of fast electrons.[20] Thus, a two-pulse driven fast electron collimation scheme is proposed, in which a guiding precursor pulse with a relatively smaller spot is adopted to generate suitable azimuthal magnetic fields that can be used to control the fast electrons generated by the main pulse with a larger spot. This has been demonstrated to be a robust fast electron collimation scheme.

It is well known that fast electrons can be confined well by a uniformly strong external axial magnetic field,[21,22] which forces them to spiral around the magnetic field lines and reduces their divergence. A 600 T magnetostatic field has been generated by a high-energy

nanosecond laser interaction with a Ni-coil target and has been applied to guide high-intensity laser-driven fast electrons, leading to efficient fast electron pinching through the solid target.[23] However, since fast electrons usually have energies of the order of several MeV, the required magnetic field has to be greater than 1000 T, and such fields are still not easy to obtain. In addition, the magnetic field is not uniform, as expected from simulations, but has a mirror-like structure, indicating that the fast electrons can be pinched by the field only if they are injected at an appropriate position,[24] otherwise they will be diffused throughout their propagation. From the resistive magnetic field generation model, it is found that the beam profile, which determines the scale length of the spatial gradient of the current, will have a significant influence on beam transport. However, to date, there have been few investigations of the effects of the beam profile.

In this paper, we study the effects of the transverse spatial profile of a fast electron beam on its transport, based on our newly developed hybrid particle-in-cell (PIC)–fluid code HEETS.[19] We first introduce the theoretical model and algorithmic method of HEETS. Then, we present the results for the transport in a silicon (Si) target of fast electron beams with transverse profiles of Gaussian, super-Gaussian, and Lorentzian form.

II. THEORETICAL MODEL

As an intense fast electron beam is transported in a dense plasma, its dynamics can be described by the Vlasov–Fokker–Planck (VFP) equation

$$\frac{\partial f_{h,e,i}}{\partial t} + \mathbf{v} \cdot \frac{\partial f_{h,e,i}}{\partial \mathbf{x}} + q_{h,e,i}(\mathbf{E} + \mathbf{v} \times \mathbf{B})\frac{\partial f_{h,e,i}}{\partial \mathbf{p}} = \left(\frac{\partial f_{h,e,i}}{\partial t}\right)_c, \quad (1)$$

where $f_{h,e,i}$ are the distribution functions of the fast electrons, background electrons, and background ions, respectively, $q_{h,e,i}$ are their charges, $\mathbf{x}$, $\mathbf{v}$, and $\mathbf{p}$ are position, velocity, and momentum, and $\mathbf{E}$ and $\mathbf{B}$ are the electric and magnetic fields. This VFP equation is extremely difficult to solve, because the independent variables constitute a six-dimensional phase space, and therefore we consider the following equivalent system of Itô stochastic differential equations (SDEs) instead:[25]

$$\frac{d\mathbf{x}}{dt} = \mathbf{v}, \quad (2)$$

$$\frac{d\mathbf{p}}{dt} = -e(\mathbf{E} + \mathbf{v} \times \mathbf{B}) + \frac{\delta \mathbf{p}}{dt}, \quad (3)$$

where $\mathbf{p} = \gamma m_e \mathbf{v}$, with γ being the Lorentz factor, and m_e is the electron mass. $\delta \mathbf{p}/dt$ is the fast electron momentum variation induced by collisions with the background electrons and ions and consists of two terms: one is the friction force term, which leads to energy loss by the fast electrons,

$$dp = \langle \Delta p \rangle \ dt = -\frac{Zn_e e^4}{4\pi\epsilon_0^2 m_e v^2} \ln \Lambda_d dt; \quad (4)$$

the other is the scattering term, which leads to variation of the transport direction,

$$d\theta = \langle \Delta\theta^2 \rangle^{1/2} \ dW = \left(\frac{Z^2 n_e e^4}{2\pi\epsilon_0^2} \frac{\gamma m_e}{p^3} \ln \Lambda_s dt\right)^{1/2} \Gamma(t), \quad (5)$$

where $dW = \Gamma(t)dt^{1/2}$ is the increment during the Wiener (i.e., diffusion) process. $\Gamma(t)$ is a random number from a Gaussian distribution with mean zero and variance one. $\ln \Lambda_d$ is the drag number and $\ln \Lambda_s$ is the scattering number, the values of which are typically in the range 5–20 and can be calculated self-consistently during the simulations. n_e is the free electron density, Z is the ionization degree, v is the fast electron velocity, and ϵ_0 is the permittivity of free space.

The background electric field is given by the generalized Ohm's law

$$\mathbf{E} = -\mathbf{u} \times \mathbf{B} + \eta\mathbf{J} - \frac{\nabla p_e}{en_e}, \quad (6)$$

where $\mathbf{u}$ is the fluid velocity, $\mathbf{J} = \mathbf{J}_i + \mathbf{J}_e$ is the total current, with $\mathbf{J}_i$ and $\mathbf{J}_e$ being the background ion and electron currents, respectively. η is the target resistivity. Since we are interested in picosecond or subpicosecond time scales, $\mathbf{J}_i$ can be neglected. The background electron current $\mathbf{J}_e$ is given by Ampère's law, i.e., $\mathbf{J}_e = (1/\mu_0)\nabla \times \mathbf{B} - \mathbf{J}_h$, where $\mathbf{J}_h$ is the fast electron current. Note that the Hall term $\mathbf{J} \times \mathbf{B}/en_e$ and the electron inertial term are not included in Eq. (6) owing to their negligible contribution in the situation that we consider here.

The magnetic field can then be obtained from the Maxwell equation

$$\frac{\partial \mathbf{B}}{\partial t} = -\nabla \times \mathbf{E}. \quad (7)$$

Combining Eqs. (6) and (7), we get

$$\frac{\partial \mathbf{B}}{\partial t} = \nabla \times (\mathbf{u} \times \mathbf{B}) - \nabla \times (\eta\mathbf{J}) + \frac{\nabla T_e \times \nabla n_e}{en_e}. \quad (8)$$

Both the second and third terms on the right-hand side of this equation generate a magnetic field: the resistive magnetic field and the Biermann battery magnetic field, respectively. The evolution of the background electron temperature is given by[19]

$$\frac{\partial}{\partial t}(C_{ve}T_e) = \eta\mathbf{J}_e^2 + \nabla \cdot (\kappa\nabla T_e) + Q_h + Q_{ie}. \quad (9)$$

Here, C_{ve} is the specific heat capacity of electrons, which, according to Ref. 26, is given by $C_{ve} = (C_{e1}^{-2} + C_{e2}^{-2})^{-1/2}$, where $C_{e1} = \frac{1}{2}\pi^2 n_e T_e/T_F$ and $C_{e2} = \frac{3}{2}n_e$ are the electron heat capacities for a degenerate and a Maxwellian plasma, respectively, with $n_e = Zn_i$, where T_F is the Fermi temperature and n_i the ion density. Although the above expression for the specific heat capacity is quite simple, it has been proved that this approach can successfully reproduce the SESAME data.[27] For the case $T_e \gg T_F$, the specific heat capacity $C_{ve} \approx \frac{3}{2}n_e$ is widely used in hybrid codes.[28,29] κ is the thermal conduction coefficient, which, for the case of isotropic thermal flux conduction, is given by

$$\kappa = \frac{16\sqrt{2}}{\pi^{3/2}} \frac{T_e^{5/2}}{Ze^4 m_e^{1/2} \ln \Lambda}.$$

$Q_h = \frac{3}{2}n_h T_h/\tau_{eh}$ is the energy obtained from the fast electrons, where

$$\tau_{eh} = \frac{3\sqrt{3}}{8\pi} \frac{m_e^{1/2} T_h^{3/2}}{n_e e^4 \ln \Lambda}$$

is the fast electron relaxation time for collisions with the background electrons. The final term in Eq. (9), Q_{ie}, is the energy exchange rate between the background electrons and ions via Coulomb collisions and can be described by the Landau formula[30] $Q_{ie} = 3m_e \nu_{ei} n_i (T_e - T_i)$, where

$$\nu_{ei} = \frac{4}{3}\left(\frac{2\pi}{m_e}\right)^{1/2}\left(\frac{q_i q_e}{4\pi\epsilon_0}\right)^2 \frac{n_i L_{ei}}{(T_e + T_i m_e/m_i)^{3/2}}$$

is the collision rate. The Coulomb logarithm is given by $L_{ei} = \ln(r_d/b_0)$, where $r_d = r_{de}r_{di}/\sqrt{r_{de}^2 + r_{di}^2}$, $r_{dj} = \nu_{Tj}/\omega_{pj}$, ν_{Tj} and ω_{pj} are the thermal velocity and plasma frequency of species j, and $b_0 = q_e q_i /[3(4\pi\epsilon_0)(T_e + T_i)]$ is the impact parameter for Coulomb collisions.

Since changes in the momentum of ions can be neglected on the picosecond time scale, we only concern ourselves with the evolution of the ion temperature and consider only energy exchange between the ions and background electrons. The ion temperature satisfies

$$\frac{\partial}{\partial t}(C_{vi} T_i) = Q_{ei}, \tag{10}$$

where C_{vi} is the specific heat capacity of ions, and $Q_{ei} = -Q_{ie}$ is the energy exchange rate between the background ions and electron via Coulomb collisions.

III. ALGORITHM METHOD

We apply the forward time centered space (FTCS) method, which is commonly employed in particle-in-cell (PIC) simulations, to solve for the fast electron velocity and position in Eqs. (2) and (3), first without the collision term and then with this term included. Considering the correction for collisions on the time step, a cutoff energy needs to be set for the fast electrons as their kinetic energy becomes small (e.g., of the order of keV) to avoid time-step limitation, especially in the case of high-Z targets. Under such conditions, we have to ignore the fast electrons. The electric and magnetic fields are defined on the Yee grid, and the leapfrog scheme is applied to solve Eqs. (6) and (7). For the background plasma temperature, the split method is employed to solve Eqs. (9) and (10), with the contribution of each term to the plasma temperature being calculated separately.

The steps of the calculation process are as follows:

1. According to experimental results for the fast electron energy spectrum, density, and angular distribution, initialize the momentum corresponding to the fast electron velocity $\mathbf{v}^{N-1/2}$, the positions $\mathbf{x}^N$ and $\mathbf{x}^{N-1}$, the initial temperatures T^{N-1} and T^N, and the electromagnetic fields $\mathbf{E}^{N-1}$, $\mathbf{B}^{N-1}$, $\mathbf{E}^N$, and $\mathbf{B}^N$, where N is the time-step number. The ionization model is used to set the initial ionization degree Z of the material and thus the density n_b^N of the background plasma.

2. For each fast electron, calculate the electromagnetic fields $\mathbf{E}_i^N$ and $\mathbf{B}_i^N$ at the position of the electron at time step N and obtain $\mathbf{v}_i^{N+1/2}$ from Eq. (3).

3. Calculate the momentum correction caused by the collision of the fast electrons with the background plasma. First, calculate the temperature T_i^N and density n_i^N at the position of the electron at the time of scattering N, and obtain $\ln \Lambda_d$, $\ln \Lambda_s$, and the corrected $\mathbf{v}_i'^{N+1/2}$ from Eqs. (4) and (5). The position $\mathbf{x}_i^{N+1/2}$ of the fast electron at the time $N + 1$ is then obtained.

4. Communicate the fast electron information, exchanging fast electrons at the boundary of the region. Boundary conditions are also applied to correct the position and momentum of the fast electrons escaping from the computational region.

5. Calculate the current deposition of fast electrons $\mathbf{J}_h^{N+1/2}$ on the grid and statistically obtain T_h^{N+1} and the number density of fast electrons n_h^{N+1}. This process requires field communication to merge the field quantities on the boundary of the region, as well as the application of boundary conditions.

6. From the temperature equation, calculate the correction terms for electron–electron collisions.

7. Use the iterative method to solve for the field quantities at time $N + 1$. Field communication and field boundary correction are required in this process.

IV. EFFECTS OF THE TRANSVERSE SPATIAL PROFILE OF THE FAST ELECTRON BEAM ON ITS TRANSPORT

We have previously studied laser-driven fast electron propagation in a Si target using PIC simulations, the results of which revealed an ionization wave propagating in the target with a velocity that was dependent on the laser intensity and was slower than the fast electron velocity.[31] However, macro-instabilities, such as filamentation instability, could not be shown, owing to limitations of time and spatial scales. Here, we mainly focus on the influence of the transverse spatial profile of a fast electron beam on its evolution within a spatial scale of a few hundreds of micrometers for several picoseconds.

The simulation box employs $250 \times 200 \times 200$ cells with a 1 μm cell size. As the laser irradiates the target, laser energy is absorbed by the target, generating fast electrons. Ponderomotive heating is the main mechanism by which electrons are heated during ultraintense laser interaction with solid targets,[32] and many theoretical and experimental results[32–34] show that the fast electron energy scales with the laser intensity. Thus, the transverse distribution of fast electrons is assumed to be consistent with the distribution of the laser intensity, for example, with $I(r) = \alpha I_0 \exp\left[-(r/r_{spot})^2\right]$ for a Gaussian laser, where $\alpha = 0.3$ is the laser absorption efficiency as reported in Ref. 35, $I_0 = 10^{20}$ W/cm^2 is the laser peak intensity, r is the radial distance from the focus center ($y = x = 0$ μm), and $r_{spot} = 9.6$ μm is the laser focal spot radius. The laser wavelength is set to $\lambda = 1.06$ μm. The temporal profile of the laser pulse is Gaussian with a duration of 1 ps (full width at half maximum, FWHM). The fast electrons are injected from the left boundary ($x = 0$) and are assumed to have an exponential energy distribution $f(E) = (1/\langle E \rangle)\exp(-E/\langle E \rangle)$, where $\langle E \rangle$ is the average energy given by the ponderomotive scaling,[32] i.e., $\langle E \rangle = m_e c^2 \left[\sqrt{1 + I(r,t)\lambda^2/1.37 \times 10^{18}} - 1\right]$, and $\langle E \rangle = 4.15$ MeV corresponds to the peak laser intensity. The initial angular distribution of fast electrons is described by $f(\theta) = \cos^M(\alpha\theta)$, where $M = 2$, $\alpha = (1/\theta_0)\cos^{-1}(0.5^{1/M})$, and $\theta_0 = 35°$ is the half width at half maximum (HWHM) of the fast electron injection angle as obtained

experimentally.[36] The target is a Si target with a density of 2.33 g/cm^3 and an initial temperature of 1 eV. The Lee–More resistivity model[37] is applied for the target resistivity, and the target ionization process is considered self-consistently using the Thomas–Fermi ionization states fitted by More.[38] Absorbing boundaries are adopted for the transverse and longitudinal boundaries for the particles and the electromagnetic fields.

Figure 1 shows the transverse profiles of the Gaussian, super-Gaussian, and Lorentzian lasers employed in this paper. When the laser irradiates the front surface of the Si target, the electrons around the surface are accelerated and propagate into the target. Note that the laser–plasma interaction process is not included in the hybrid code, and the characteristics of the fast electron beam are directly given by the abovementioned theoretical and experimental results. The super-Gaussian laser has a sharp periphery, while the Lorentzian laser has a much slower decreasing profile along the radial direction compared with the other profiles. Although the laser energies are close for the three transverse profiles, we will see later that the differences in the laser profiles can induce significant differences in the fast electron beam propagation in the target.

Figure 2 shows the transverse distributions of fast electron density at $t = 1.6$ ps for a Gaussian laser-driven electron beam propagating in the Si target. It can be seen that the transverse distribution of the fast electron beam expands with increasing penetration depth owing to its initial divergence. The fast electron beam has a uniform distribution in the region $x = 1$–50 μm, while filaments appear
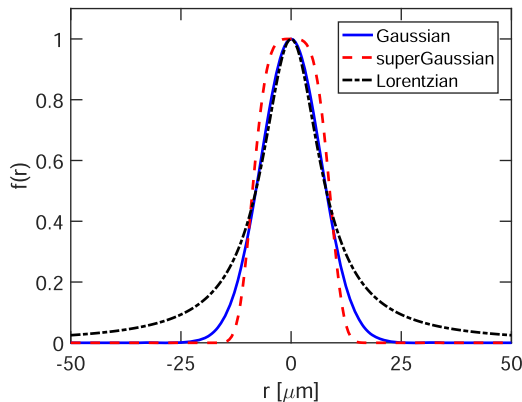

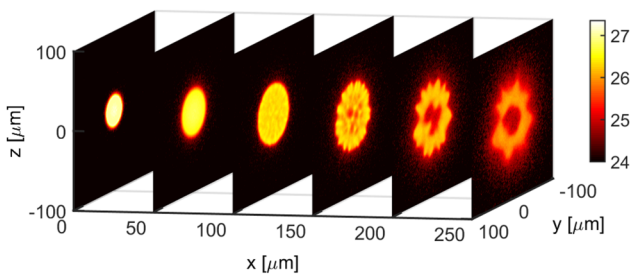FIG. 1. Transverse profiles of Gaussian, super-Gaussian, and Lorentzian lasers.

FIG. 2. Transverse distributions of denary logarithm of fast electron density at $t = 1.6$ ps. The density in this and the other figures is in units of m^{-3}.

after it has penetrated $x = 100$ μm into the slice. This filamentation becomes more pronounced as the penetration depth increases, resembling an octopus structure.

Figure 3 shows the longitudinal distributions of fast electron density, target resistivity, and magnetic field B_y at $t = 1.0$ and 1.6 ps, respectively. It can be seen from Figs. 3(a) and 3(b) that fast electron filaments begin to appear after $x = 100$ μm, accompanied by the generation of magnetic fields of about 80 T. The target has a higher resistivity around the electron beam and filaments, since there is higher ionization but a lower target temperature there compared with the region of the target around the laser propagation axis. The maximum resistivity is around 4×10^{-6} Ω·m. The resistive magnetic field $\mathbf{B} \propto \eta \mathbf{J}/Lt$ reaches 1026 T at the periphery of the fast electron beam at $x = 90$ μm at $t = 1.6$ ps, as shown in Figs. 3(e) and 3(f), where L is the characteristic length of spatial variation of the resistivity/fast electron current density. The self-generated magnetic field strongly pinches the fast electron beam. Thus, the cone angle of the fast electron distribution is much smaller than the initial divergence.

Figure 4 shows the background electron and ion temperatures at $t = 1.6$ ps. The heating of a solid target is mainly Ohmic, i.e., $\eta \mathbf{J}^2$, which, owing to the moderate target density, is a much more efficient heating mechanism than the direct collision of fast electrons with the background electrons.[21] Fast electron energy is deposited first to the background electrons, and then energy is transferred from the electrons to the background ions by collisions. It can be seen that the electron temperature around the laser injection position can reach 1469 eV, while the maximum ion temperature is 808 eV. The temperature of the background electrons is always higher than that of the ions along the propagation path of fast electron transport, as shown in Fig. 4(c), indicating that the ions and electrons are not in equilibrium. Since the electron–ion collision frequency ν_{ei} scales with $T_e^{-3/2}$, the temperature difference between electrons and ions becomes smaller as the fast electrons penetrate deeper into the target, owing to the lower fast electron current density and thus the reduced target heating efficiency, leading to a higher frequency of electron–ion collisions.

To see clearly the effect of the transverse profile of the fast electron beam on its propagation, we model the transport of the fast electron beams produced in the Si target by super-Gaussian (fourth-order) and Lorentzian lasers with respective intensity distributions $I(r) = \alpha I_0 \exp\left[-(r/r_{\text{spot}})^4\right]$ and $I(r) = \alpha I_0 \Gamma^2/(r^2 + \Gamma^2)$, where Γ is the HWHM. The transverse distributions of the fast electron density for super-Gaussian and Lorentzian laser injection at $t = 1.6$ ps are shown in Fig. 5. It can be seen that the fast electrons produced by the super-Gaussian laser are pinched to a much smaller spot than those produced by the Lorentzian laser. However, in the case of the super-Gaussian laser, owing to the stronger pinching of the fast electron beam by the resistive magnetic field, there is a higher electron current, allowing more filaments to be observed. The Lorentzian laser-driven electron beam has a much more uniform distribution, and so obvious filaments only appear deeper (~200 μm) in the target. Owing to the weak confinement of the resistive magnetic field, the fast electrons have a widely spread spot at the rear of the target ($x = 250$ μm).

In Fig. 6, the longitudinal distributions of fast electron density, target resistivity, and magnetic field B_y for super-Gaussian and Lorentzian laser injection at $t = 1.6$ ps are presented. It can be
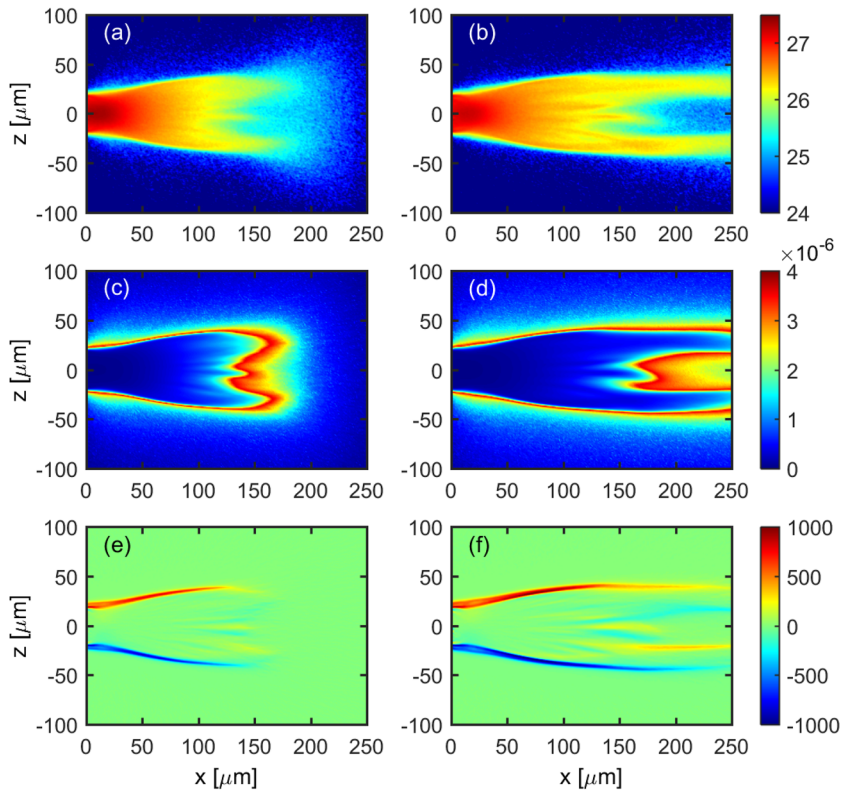
FIG. 3. Longitudinal distributions of denary logarithm of fast electron density [(a) and (b)], target resistivity [(c) and (d)], and magnetic field B_y [(e) and (f)] at t = 1.0 ps [(a), (c), and (e)] and 1.6 ps [(b), (d), and (f)]. The resistivity and magnetic field in this and the other figures are in units of $\Omega \cdot$m and T, respectively.
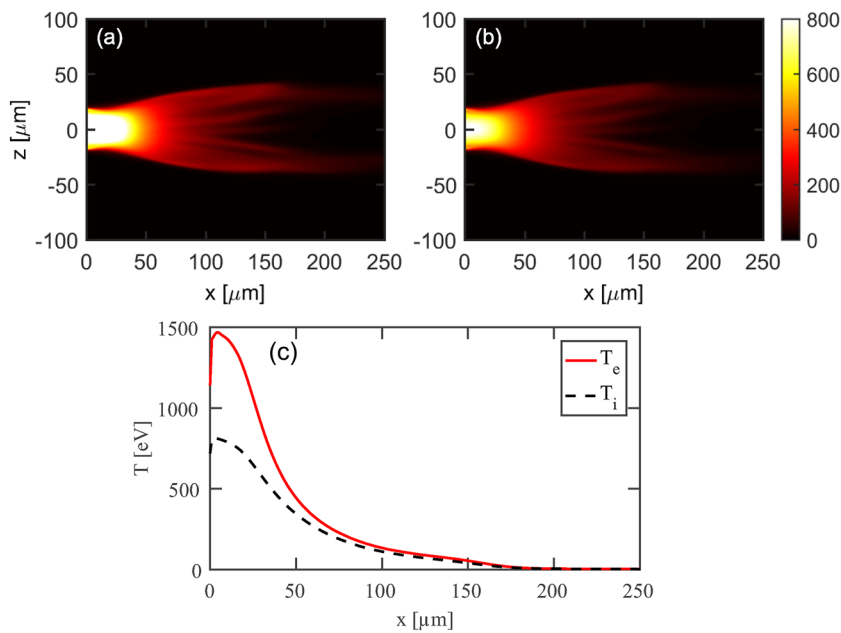

FIG. 4. Longitudinal distributions of background electron temperature (a) and ion temperature (b) at t = 1.6 ps and the corresponding temperature profile along the x direction around the z axis (c). The temperature is in units of eV.
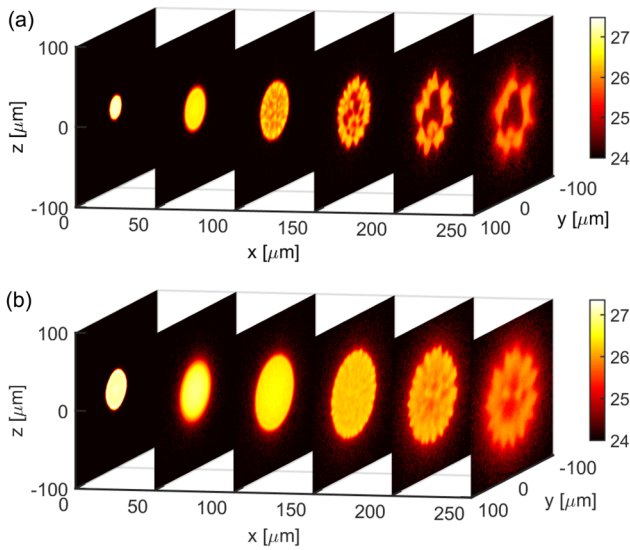
FIG. 5. Transverse distributions of denary logarithm of fast electron density for super-Gaussian (a) and Lorentzian (b) laser injection at t = 1.6 ps.

seen that obvious filaments appear after x = 50 μm for the super-Gaussian laser, whereas the fast electrons do not begin to separate into filaments until x = 150 μm for the Lorentzian laser. Similar filamentation behavior can be seen in the resistivity distributions. We see that the depth at which filaments appear decreases with increasing transverse spatial gradient of the laser profile. The resistivity filaments only appear when the fast electrons have propagated to the rear of the target. The accompanying resistive magnetic field around the filaments can reach 400 T, which is five times that in the case of the Gaussian laser. The magnetic field reaches 1029 T at the periphery of the fast electron beam at x = 90 μm. This is close in magnitude to the magnetic field of the Gaussian laser, but it has a much more uniform distribution deep into the target and thus imposes a stronger pinch on the fast electron beam. The magnetic field in the Lorentzian case is only around 689 T, inducing a weak pinch effect.

We have developed a collimation criterion for fast electron propagation in dense plasmas, with the resistive magnetic field values required to achieve electron collimation being described by Eq. (9) in Ref. 19. The situation described here in which fast electrons are reflected by the magnetic field corresponds to case (a) in Ref. 19, as given by

$$d > d_1,$$
$$L > 2r_0 \sin \frac{1}{2}\theta + L_2. \tag{11}$$

Here, d and L are the transverse width and longitudinal length, respectively, of the self-generated magnetic field,

$$d_1 = r_0\left(1 - \cos\frac{1}{2}\theta\right), \qquad L_2 = \frac{R\cos\theta}{\sin|\theta - \alpha|},$$
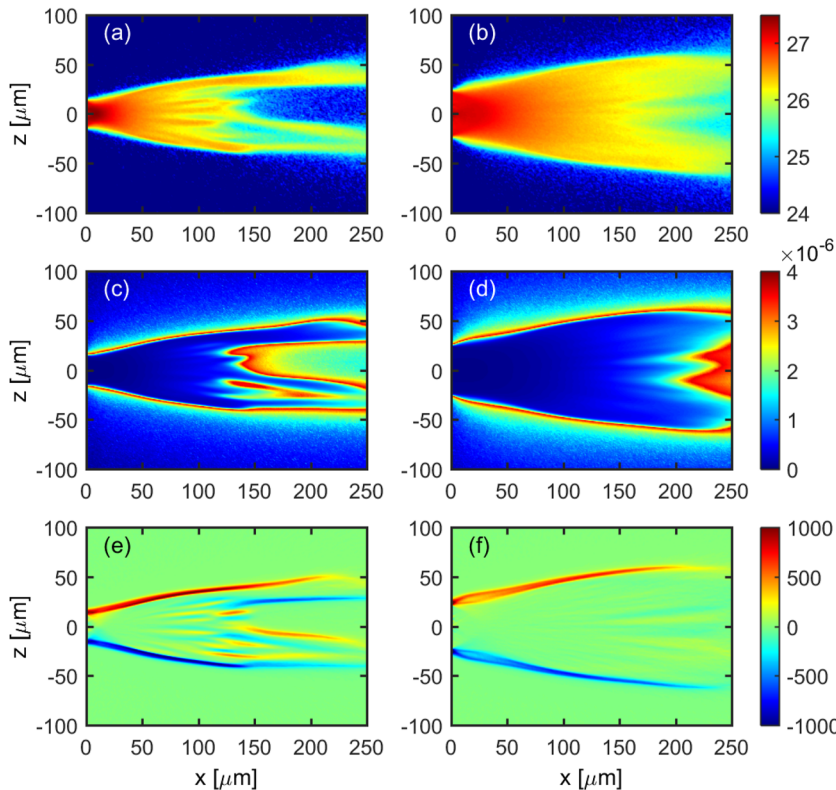

FIG. 6. Longitudinal distributions of denary logarithm of fast electron density [(a) and (b)], target resistivity [(c) and (d)], and magnetic field B_y [(e) and (f)] at t = 1.6 ps for super-Gaussian [(a), (c), and (e)] and Lorentzian [(b), (d), and (f)] laser injection.
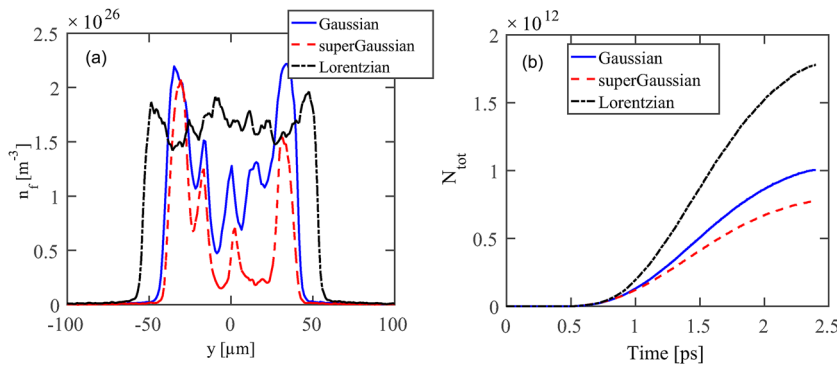
FIG. 7. Transverse profiles of denary logarithm of fast electron density at $x = 150$ μm (a) and the number of fast electrons penetrating through an area of radius 55 μm at the slice $x = 150$ μm (b).

and $r_0 = \gamma_0 m_e v_0 / eB_\phi$ is the Larmor radius, with v_0, e, m_e, and γ_0 being the fast electron velocity, charge, mass, and Lorentz factor, respectively. θ is fast electron initial divergence and α is the tilt angle of the resistive magnetic field. R is the transverse offset of the fast electron injection position with respect to the magnetic field layer. When the tilt angle of the magnetic field approaches the fast electron divergence, i.e., $\alpha \to \theta$, then $L_2 \to \infty$, and so L becomes very large. We can see that even for the Gaussian laser, the width (FWHM) of the magnetic field is ~5 μ m (around $x = 50$ μm), which satisfies the condition in (11), but the length of the magnetic field is much greater than that in (11) (i.e., 11 μm for $B_\phi = 710$ T) at $t = 1$ ps. The magnetic field becomes stronger in the case of the super-Gaussian laser, and so the confinement of the fast electrons by the magnetic field is enhanced. The fast electrons can also be confined by the magnetic field around the injection region in the case of the Lorentzian laser, where the width and magnitude of the magnetic field reach 6 μm and 500 T at $t = 0.8$ ps, but the fast electron trajectories diverge later as the magnetic field becomes weak, and the conditions in (11) cannot be satisfied.

Fast Fourier transformation of the resistive magnetic fields B_y shown in Figs. 3 and 6 reveals the existence of an oblique instability mode, and the oblique angle increases with decreasing transverse spatial gradient of the laser: 77° for the super-Gaussian laser and 80° for the Lorentzian laser. The instability is strongest in the case of the super-Gaussian laser, in which the transverse wave number increases to become as large as π μm^{-1}. This instability can be attributed to filamentation instability, as reported in Refs. 39 and 40, but it is not a purely transverse mode, and longitudinal modes also grow. The transverse spatial profile of the electron beam does indeed affect the growth rate of the instability, which can be weakened by making the spatial density gradient more gentle.

From the transverse profile of the fast electrons at the slice $x = 150$ μm [Fig. 7(a)], it can be seen that the tendency to filamentation of the fast electron beam becomes much stronger as the transverse distribution becomes steeper. The profiles of the fast electron distributions in the deep target become hollow for both the cases of Gaussian and super-Gaussian lasers. This can be attributed to the steep current density in these two cases, producing a more intense resistive magnetic field that repels the fast electron current by the return current. Although the areal density of the Si target here is only $\rho R \approx 0.06$ g/cm^2, which is much smaller than the fast electron penetration range corresponding to

the mean energy ($\langle E \rangle = 4.15$ MeV), a large fraction of fast electrons with low energies (due to the exponential energy spectrum) are stopped in the target both by the resistive fields and by collisions, as can be seen in Fig. 7(b). The total number of fast electrons penetrating through the slice $x = 150$ μm increases in the case of a more slowly increasing transverse profile. This indicates that the transverse spatial profile of the fast electron beam has a significant influence on its propagation, and we can control the propagation of a fast electron beam in a target by modulating the spatial profile of the laser.

The temperature profiles of electrons and ions along the x axis around the central axis are also investigated for the Gaussian, super-Gaussian, and Lorentzian lasers (however, for brevity, the results are not shown). The target electrons are heated to a higher temperature around the laser injection position for the super-Gaussian laser. This can be attributed to the fact that higher fast electron current density for the super-Gaussian laser, due to the strong pinching by the resistive magnetic field, leads to efficient Ohmic heating of the target. However, because the fast electron current tends to become filamented in the deep target, and we have cut off the laser as its intensity decreases to $0.1I_0$ in the radial direction to reduce the computational burden, the total input electron energy for the Lorentzian laser is somewhat higher than that in the other cases. Thus, both the electron and ion temperatures in the deep target for the Lorentzian laser are higher than those in the other cases. It is also found that the electromagnetic field energy in the case of the super-Gaussian laser is about 1.35 times that in the case of the Lorentzian laser, i.e., more fast electron energy is transferred to the electromagnetic fields. This is consistent with the magnetic field distributions in Fig. 6.

It is worth mentioning that although the hybrid PIC–fluid model can simulate larger spatial and time scales than PIC simulations are able to do, microphysical processes, such as two-stream and Weibel instabilities, are not modeled in the simulations. The influence of such micro-instabilities can be approximately accounted for by a suitable choice of resistivity. In addition, the laser–solid interaction process is not included, meaning that accurate description of the fast electron characteristics is quite important to reflect the realistic process of fast electron transport. To characterize the fast electrons accurately, their density, divergence, energy, temperature, etc., need to be extracted from accurate PIC simulations or experimental results.

V. CONCLUSION

Fast electrons driven by ultra-intense laser propagation in a silicon target have been studied by hybrid PIC–fluid simulations. We have found that the transverse spatial profile of the fast electron beam can significantly affect the propagation of these electrons. Fast electrons are pinched tightly by the resistive magnetic field in the case of a super-Gaussian profile, which also leads to a greater tendency to filamentation. In the case of a Lorentzian profile, the fast electron beam spreads widely in the target owing to the weaker confining magnetic field. We can modulate the spatial profile of the laser to control fast electron propagation. The findings of this study should be helpful for laser-driven fast electron applications, especially with regard to the fast ignition of inertial confinement fusion.

ACKNOWLEDGMENTS

AUTHOR DECLARATIONS

Conflict of Interest

The authors have no conflicts to disclose.

Author Contributions

X. H. Yang: Conceptualization (lead); Formal analysis (lead); Funding acquisition (equal); Investigation (equal); Methodology (equal); Software (equal); Writing – original draft (lead); Writing – review & editing (lead). **Z. H. Chen**: Data curation (equal); Visualization (supporting). **H. Xu**: Conceptualization (equal); Methodology (equal); Software (equal); Writing – review & editing (equal). **Y. Y. Ma**: Formal analysis (equal); Funding acquisition (equal); Writing – review & editing (supporting). **G. B. Zhang**: Data curation (equal); Writing – review & editing (supporting). **D. B. Zou**: Formal analysis (supporting); Methodology (supporting). **F. Q. Shao**: Methodology (equal); Supervision (equal).

DATA AVAILABILITY

The data that support the findings of this work are available from the corresponding author upon reasonable request.

REFERENCES

[1]M. Tabak, J. Hammer, M. E. Glinsky, W. L. Kruer, S. C. Wilks, J. Woodworth, E. M. Campbell, M. D. Perry, and R. J. Mason, "Ignition and high gain with ultrapowerful lasers," Phys. Plasmas **1**, 1626 (1994).

[2]X. H. Yang, H. B. Zhuo, H. Xu, Z. Y. Ge, F. Q. Shao, M. Borghesi, and Y. Y. Ma, "Effects of filamentation instability on the divergence of relativistic electrons driven by ultraintense laser pulses," Phys. Plasmas **23**, 103110 (2016).

[3]A. Debayle, J. J. Honrubia, E. d'Humières, and V. T. Tikhonchuk, "Divergence of laser-driven relativistic electron beams," Phys. Rev. E **82**, 036405 (2010).

[4]V. M. Ovchinnikov, D. W. Schumacher, M. McMahon, E. A. Chowdhury, C. D. Chen, A. Morace, and R. R. Freeman, "Effects of preplasma scale length and laser intensity on the divergence of laser-generated hot electrons," Phys. Rev. Lett. **110**, 065007 (2013).

[5]L. Gremillet, D. Bénisti, E. Lefebvre, and A. Bret, "Linear and nonlinear development of oblique beam-plasma instabilities in the relativistic kinetic regime," Phys. Plasmas **14**, 040704 (2007).

[6]B. Hao, W. J. Ding, Z. M. Sheng, C. Ren, X. Kong, J. Mu, and J. Zhang, "Collisional effects on the oblique instability in relativistic beam-plasma interactions," Phys. Plasmas **19**, 072709 (2012).

[7]A. Bret, "Weibel, two-stream, filamentation, oblique, Bell, Buneman...which one grows faster?," Astrophys. J **699**, 990–1003 (2009).

[8]P. Norreys, D. Batani, S. Baton, F. N. Beg, R. Kodama, P. M. Nilson, P. Patel, F. Pérez, J. J. Santos, R. H. H. Scott, V. T. Tikhonchuk, M. Wei, and J. Zhang, "Fast electron energy transport in solid density and compressed plasma," Nucl. Fusion **54**, 054004 (2014).

[9]A. P. L. Robinson, M. Sherlock, and P. A. Norreys, "Artificial collimation of fast-electron beams with two laser pulses," Phys. Rev. Lett. **100**, 025002 (2008).

[10]C. T. Zhou, L. Y. Chew, and X. T. He, "Propagation of energetic electrons in a hollow plasma fiber," Appl. Phys. Lett. **97**, 051502 (2010).

[11]Y. Zeng, Y. Tian, C. Zhou, Z. Li, J. Liu, and Z. Xu, "Experimental study on laser-driven electron collimation along wire targets," Phys. Plasmas **26**, 012701 (2019).

[12]D. A. MacLellan, D. C. Carroll, R. J. Gray, N. Booth, M. Burza, M. P. Desjarlais, F. Du, D. Neely, H. W. Powell, A. P. L. Robinson, G. G. Scott, X. H. Yuan, C.-G. Wahlström, and P. McKenna, "Tunable mega-ampere electron current propagation in solids by dynamic control of lattice melt," Phys. Rev. Lett. **113**, 185001 (2014).

[13]X. Vaisseau, A. Morace, M. Touati, M. Nakatsutsumi, S. D. Baton, S. Hulin, P. Nicolaï, R. Nuter, D. Batani, F. N. Beg, J. Breil, R. Fedosejevs, J.-L. Feugeas, P. Forestier-Colleoni, C. Fourment, S. Fujioka, L. Giuffrida, S. Kerr, H. S. McLean, H. Sawada, V. T. Tikhonchuk, and J. J. Santos, "Collimated propagation of fast electron beams accelerated by high-contrast laser pulses in highly resistive shocked carbon," Phys. Rev. Lett. **118**, 205001 (2017).

[14]R. B. Campbell, J. S. DeGroot, T. A. Mehlhorn, D. R. Welch, and B. V. Oliver, "Collimation of laser-generated relativistic electron beams propagating through solid matter," Phys. Plasmas **10**, 4169 (2003).

[15].H. B. Cai, K. Mima, W. M. Zhou, T. Jozaki, H. Nagatomo, A. Sunahara, and R. J. Mason, "Enhancing the number of high-energy electrons deposited to a compressed pellet via double cones in fast ignition," Phys. Rev. Lett **102**, 245001 (2009).

[16]X. H. Yang, H. Xu, Y. Y. Ma, F. Q. Shao, Y. Yin, H. B. Zhuo, M. Y. Yu, and C. L. Tian, "Propagation of attosecond electron bunches along the cone-and-channel target," Phys. Plasmas **18**, 023109 (2011).

[17]R. Kodama, Y. Sentoku, Z. L. Chen, G. R. Kumar, S. P. Hatchett, Y. Toyama, T. E. Cowan, R. R. Freeman, J. Fuchs, Y. Izawa, M. H. Key, Y. Kitagawa, K. Kondo, T. Matsuoka, H. Nakamura, M. Nakatsutsumi, P. A. Norreys, T. Norimatsu, R. A. Snavely, R. B. Stephens, M. Tampo, K. A. Tanaka, and T. Yabuuchi, "Plasma devices to guide and collimate a high density of MeV electrons," Nature **432**, 1005 (2004).

[18]S. Kar, A. P. L. Robinson, D. C. Carroll, O. Lundh, K. Markey, P. McKenna, P. Norreys, and M. Zepf, "Guiding of relativistic electron beams in solid targets by resistively controlled magnetic fields," Phys. Rev. Lett. **102**, 055001 (2009).

[19]H. Xu, X. H. Yang, J. Liu, and M. Borghesi, "Control of fast electron propagation in foam target by high-Z doping," Plasma Phys. Controlled Fusion **61**, 025010 (2019).

[20]H. Xu, X. H. Yang, Z. M. Sheng, P. McKenna, Y. Y. Ma, H. B. Zhuo, Y. Yin, C. Ren, and J. Zhang, "Collimation of high-current fast electrons in dense plasmas with a tightly focused precursor intense laser pulse," Nucl. Fusion **59**, 126024 (2019).

[21]X. H. Yang, H. Xu, Y. Y. Ma, Z. Y. Ge, H. B. Zhuo, and F. Q. Shao, "Energy deposition of fast electrons in dense magnetized plasmas," Phys. Plasmas **25**, 063104 (2018).

[22]W. M. Wang, P. Gibbon, Z. M. Sheng, and Y. T. Li, "Magnetically assisted fast ignition," Phys. Rev. Lett. **114**, 015001 (2015).

[23]M. Bailly-Grandvaux, J. J. Santos, C. Bellei, P. Forestier-Colleoni, S. Fujioka, L. Giuffrida, J. J. Honrubia, D. Batani, R. Bouillaud, M. Chevrot, J. E. Cross, R. Crowston, S. Dorard, J.-L. Dubois, M. Ehret, G. Gregori, S. Hulin, S. Kojima, E. Loyez, J.-R. Marquès, A. Morace, P. Nicolaï, M. Roth, S. Sakata, G. Schaumann, F. Serres, J. Servel, V. T. Tikhonchuk, N. Woolsey, and Z. Zhang, "Guiding of relativistic electron beams in dense matter by laser driven magnetostatic fields," Nat. Commun. **9**, 102 (2018).

[24]Y. Cao, X. H. Yang, T. P. Yu, Y. Y. Ma, M. Y. Yu, L. X. Hu, G. B. Zhang, H. Xu, and Y. Lang, "Transport of fast electron beam in mirror-field magnetized solid-density plasma," Phys. Plasmas **28**, 102701 (2021).

[25]J. R. Davies, A. R. Bell, M. G. Haines, and S. M. Guérin, "Short-pulse high-intensity laser-generated fast electron transport into thick solid targets," Phys. Rev. E **56**, 7193 (1997).

[26]P. Antici, L. Gremillet, T. Grismayer, P. Mora, P. Audebert, M. Borghesi, C. A. Cecchetti, A. Mančic, and J. Fuchs, "Modeling target bulk heating resulting from ultra-intense short pulse laser irradiation of solid density targets," Phys. Plasmas **20**, 123116 (2013).

[27]K. Eidmann, J. Meyer-ter-Vehn, T. Schlegel, and S. Hüller, "Hydrodynamic simulation of subpicosecond laser interaction with solid-density matter," Phys. Rev. E **62**, 1202 (2000).

[28]A. P. L. Robinson, H. Schmitz, and P. McKenna, "Resistivity of non-crystalline carbon in the 1–100 eV range," New J. Phys. **17**, 083045 (2015).

[29]D. J. Strozzi, M. Tabak, D. J. Larson, L. Divol, A. J. Kemp, C. Bellei, M. M. Marinak, and M. H. Key, "Fast-ignition transport studies: Realistic electron source, integrated particle-in-cell and hydrodynamic modeling, imposed magnetic fields," Phys. Plasmas **19**, 072711 (2012).

[30]L. Spitzer, *Physics of Fully Ionized Gasses* (Wiley, 1962).

[31]X. H. Yang, C. Ren, H. Xu, Y. Y. Ma, and F. Q. Shao, "Transport of ultraintense laser-driven relativistic electrons in dielectric targets," High Power Laser Sci. Eng. **8**, e2 (2020).

[32]S. C. Wilks, W. L. Kruer, M. Tabak, and A. B. Langdon, "Absorption of ultra-intense laser pulse," Phys. Rev. Lett. **69**, 1383 (1992).

[33]F. N. Beg, A. R. Bell, A. E. Dangor, C. N. Danson, A. P. Fews, M. E. Glinsky, B. A. Hammel, P. Lee, P. A. Norreys, and M. Tatarakis, "A study of picosecond laser-solid interactions up to 10^{19} W/cm^2," Phys. Plasmas **4**, 447 (1997).

[34]M. G. Haines, M. S. Wei, F. N. Beg, and R. B. Stephens, "Hot-electron temperature and laser-light absorption in fast ignition," Phys. Rev. Lett. **102**, 045008 (2009).

[35]J. R. Davies, "Laser absorption by overdense plasmas in the relativistic regime," Plasma Phys. Controlled Fusion **51**, 014006 (2009).

[36]J. S. Green, V. M. Ovchinnikov, R. G. Evans, K. U. Akli, H. Azechi, F. N. Beg, C. Bellei, R. R. Freeman, H. Habara, R. Heathcote, M. H. Key, J. A. King, K. L. Lancaster, N. C. Lopes, T. Ma, A. J. MacKinnon, K. Markey, A. McPhee, Z. Najmudin, P. Nilson, R. Onofrei, R. Stephens, K. Takeda, K. A. Tanaka, W. Theobald, T. Tanimoto, J. Waugh, L. Van Woerkom, N. C. Woolsey, M. Zepf, J. R. Davies, and P. A. Norreys, "Effect of laser intensity on fast-electron-beam divergence in solid-density plasmas," Phys. Rev. Lett. **100**, 015003 (2008).

[37]Y. T. Lee and R. M. More, "An electron conductivity model for dense plasmas," Phys. Fluids **27**, 1273 (1984).

[38]R. M. More, "Pressure ionization, resonances, and the continuity of bound and free states," Adv. At. Mol. Phys. **21**, 305–356 (1985).

[39]L. Gremillet, G. Bonnaud, and F. Amiranoff, "Filamented transport of laser-generated relativistic electrons penetrating a solid target," Phys. Plasmas **9**, 941 (2002).

[40]A. Bret, M.-C. Firpo, and C. Deutsch, "Characterization of the initial filamentation of a relativistic electron beam passing through a plasma," Phys. Rev. Lett. **94**, 115002 (2005).